Electronic Supplementary Information

Organometallic phosphors as building blocks in sol-gel chemistry. Luminescent organometallo-silica materials.

*C. Ezquerro,[a] A.E. Sepúlveda,[a] A. Grau-Atienza,[b] E. Serrano,[b] E. Lalinde,[a] J. R. Berenguer,[*a] J. García-Martínez[*b]*

[a] *Departamento de Química-Centro de Investigación en Síntesis Química (CISQ), Universidad de La Rioja, Madre de Dios, 51, E-26006,Logroño, Spain. Tel: +34 941299646; *E-mail: jesus.berenguer@unirioja.es, URL: https://cisq.unirioja.es/gmmo.php*

[b] *Laboratorio de Nanotecnología Molecular. Departamento de Química Inorgánica. Universidad de Alicante, Carretera San Vicente s/n, E-03690, Alicante, Spain. Fax: +34 965903454; Tel: +34 965903400 ext.2224; *E-mail: j.garcia@ua.es, URL: www.nanomol.es*

General methods

IR spectra were recorded on a Nicolet Nexus FT-IR Spectrometer in a wavenumber range from 4000 to 200 cm^{-1}. All samples were prepared as KBr pellets. Elemental analyses were carried out in a Perkin-Elmer 2400 CHNS/O and a Thermo Finnigan Flash 1112 microanalyzer. Mass spectra were recorded on a Microflex MALDI-TOF Bruker spectrometer. NMR spectra were recorded on Bruker ARX300 and ARX400 spectrometers. Chemical shifts are reported in parts per million (ppm) relative to external standards ($SiMe_4$ for ^1H and $^{13}C\{^1H\}$, $CFCl_3$ for ^{19}F and H_3PO_4 for $^{31}P\{^1H\}$) and coupling constants in Hz. ^1H and $^{13}C\{^1H\}$ NMR spectra were assigned, following the numbering scheme shown in Figure S1, by means of 2D experiments (^1H-^1H COSY and ^1H-^{13}C HSQC and HMBC) dinuclear. UV-Vis spectra in solution were recorded on an Agilent 8453 spectrophotometer. Diffuse Reflectance UV-vis (DRUV) spectra were carried out in KBr pellets, using a Shimazdu UV-3600 spectrophotometer with a Harrick praying mantis accessory, and recalculated following the Kubelka Munk function. The excitation and emission spectra were obtained on a Jobin-Yvon Horiba Fluorolog 3-11 Tau-3 spectrofluorimeter. The lifetime measurements were performed operating in the phosphorimeter mode (with a F1-1029 lifetime emission PMT assembly, using a 450 W Xe lamp) or with a Datastation HUB-B with a nanoLED controller and software DAS6. The nano-LEDs employed for lifetime measurements were of wavelength 370 nm with pulse lengths of 0.8−1.4 ns. The lifetime data were fitted using the Jobin-Yvon software package. Quantum yields in solid were measured using a F-3018 Integrating Sphere mounted on the Fluorolog 3-11 Tau-3 spectrofluorimeter.

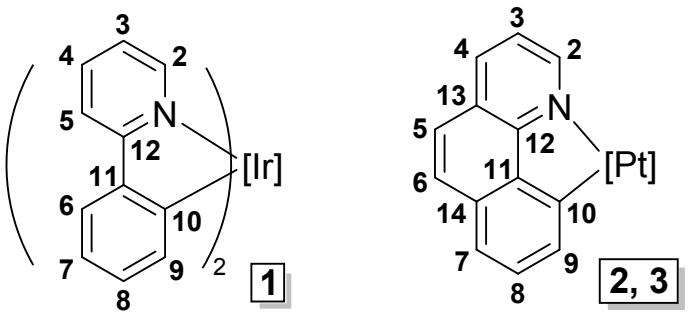

Figure S1. Schematic view of complexes **1** – **3**, showing the numbering scheme used in the NMR characterization (see General methods).

For a successful characterization of all the silica-based hybrid materials, the silica gels were also previously air dried at room temperature. Metal contents were determined by high resolution inductively coupled plasma mass spectrometry (HR-ICP-MS, ELEMENT XR). The samples were dissolved in a mixture of 3,5 ml HCl + 1 ml HNO3 + 1 mL HF + 5mL H_3BO_3 (5%), digested in a microwave (260ºC, 45 bar) and filtered off (0.45 μm) prior to analysis. This treatment is able to entirely dissolve the samples. The morphology of the mesoporous materials was investigated by transmission electron microscopy (TEM) and scanning electron microscopy (SEM). Both electron diffraction experiments and TEM images were performed using a JEM-2010 microscope (JEOL, 0.14 nm of resolution), at an accelerating voltage of 200 kV. Samples for TEM studies were prepared by dipping a sonicated suspension of the sample in ethanol on a carbon-coated copper. The digital analysis of the TEM micrographs was performed using DigitalMicrographTM 3.6.1. by Gatan. SEM analyses were carried out in a field emission scanning electron microscope (FESEM) Merlin VP Compact (Zeiss, 1.6 nm of resolution at 1 kV). Porous texture was characterized by nitrogen sorption measurements at 77 K in an AUTOSORB-6 apparatus. The samples were previously degassed at 373 K for 4 h and 5 × 10−5 bars. Adsorption data were analysed using the software QuadraWinTM (version 6.0) of Quantachrome Instruments. The BET surface area was estimated by using multipoint BET method, using the adsorption data in the relative pressure (P/P0) range of 0.05–0.20. Cumulative pore volumes and pore-size distribution curves were calculated using the DFT method (NLDFT adsorption branch model, which assumes nitrogen adsorption at 77 K in cylindrical silica pores for the mesopore range).[1] The total pore volume was obtained at the plateau of the cumulative adsorption pore volume plot (the micropore volume was determined by using t-plot method to be 0), see Figure S3.

X-ray diffraction structure of [Pt(bzq)(C_6F_5)(PPETS)] (2)

Yellow crystals of complex **2** were obtained by slow diffusion of *n*-hexane in a saturated dichloromethane solution of the complex at room temperature. X-ray intensity data were collected with a NONIUS-κCCD area-detector diffractometer, using graphite-monochromated Mo K_α radiation (λ(MoK_α) 0.71071 Å) and the images were processed using the DENZO and SCALEPACK suite of programs,[2] making the absorption correction at this point. The structure was solved by intrinsic phasing using SHELXT[3] and refined by full-matrix least squares on F^2 with SHELXL.[4] All non-hydrogen atoms were assigned anisotropic displacement parameters. The hydrogen atoms were constrained to idealized geometries fixing isotropic displacement parameters of 1.2 times the U_{iso} value of their attached carbons for aromatic and methylene hydrogens and 1.5 times for the methyl groups. One of the terminal ethyl groups of the phosphine ligand presented positional disorder and was modeled adequately (C37, C38; occupancy 0.75/0.25).

Table S1a. Selected bond lengths (Å) and angles (°) for [Pt(bzq)(C_6F_5)(PPETS)] **(2)**.

Pt(1)-N(1)	2.105(3)	Pt(1)-P(1)	2.3248(8)
Pt(1)-C(10)	2.051(3)	Pt(1)-C(15)	1.998(3)
N(1)-Pt(1)-C(10)	80.3(1)	N(1)-Pt(1)-P(1)	99.21(8)
C(10)-Pt(1)-C(15)	90.0(1)	C(15)-Pt(1)-P(1)	90.49(8)
C(15)-Pt(1)-N(1)	170.2(1)	C(10)-Pt(1)-P(1)	178.01(9)

Table S1b. Crystallographic data for [Pt(bzq)(C_6F_5)(PPETS)] **(2).**

Empirical formula	$C_{39}H_{37}F_5NO_3PPtSi$
F_w	916.84
T (K)	173(1) K
crystal system, space group	Triclinic, *P*-1
a(Å)	12.2141(5)
b(Å)	12.5271(4)
c(Å)	12.7251(5)
α(deg)	75.765(3)
β(deg)	84.072(2)0
γ(deg)	71.946(3
volume (A^3)	1793.6(1)
Z	2
D_{calcd} (Mg/m^3)	1.698
absorption coefficient (mm^{-1})	4.055
F(000)	908
θ range for data collection (deg)	3.305 to 27.471
no of data // restraints // params	7719 // 0 // 478
goodness-of-fit on $F^{2[a]}$	1.089
final R indexes [$I>2\sigma(I)$][a]	R_1 = 0.0296, wR_2 = 0.0812
R indexes (all data)[a]	R_1 = 0.0306, wR_2 = 0.0821
largest diff peak and hole ($e\cdot Å^{-3}$)	1.129 and -1.881

[a] $R1 = \Sigma(\left|F_o\right| - \left|F_c\right|)/\Sigma\left|F_o\right|$; $wR2 = [\Sigma w(F_o^2 - F_c^2)^2/\Sigma wF_o^2]^{1/2}$; goodness of fit = $\{\Sigma[w(F_o^2 - F_c^2)^2]/(N_{obs} - N_{param})\}^{1/2}$; $w = [\sigma^2(F_o) + (g_1P)^2 + g_2P]^{-1}$; $P = [\max(F_o^2;0 + 2F_c^2]/3$.

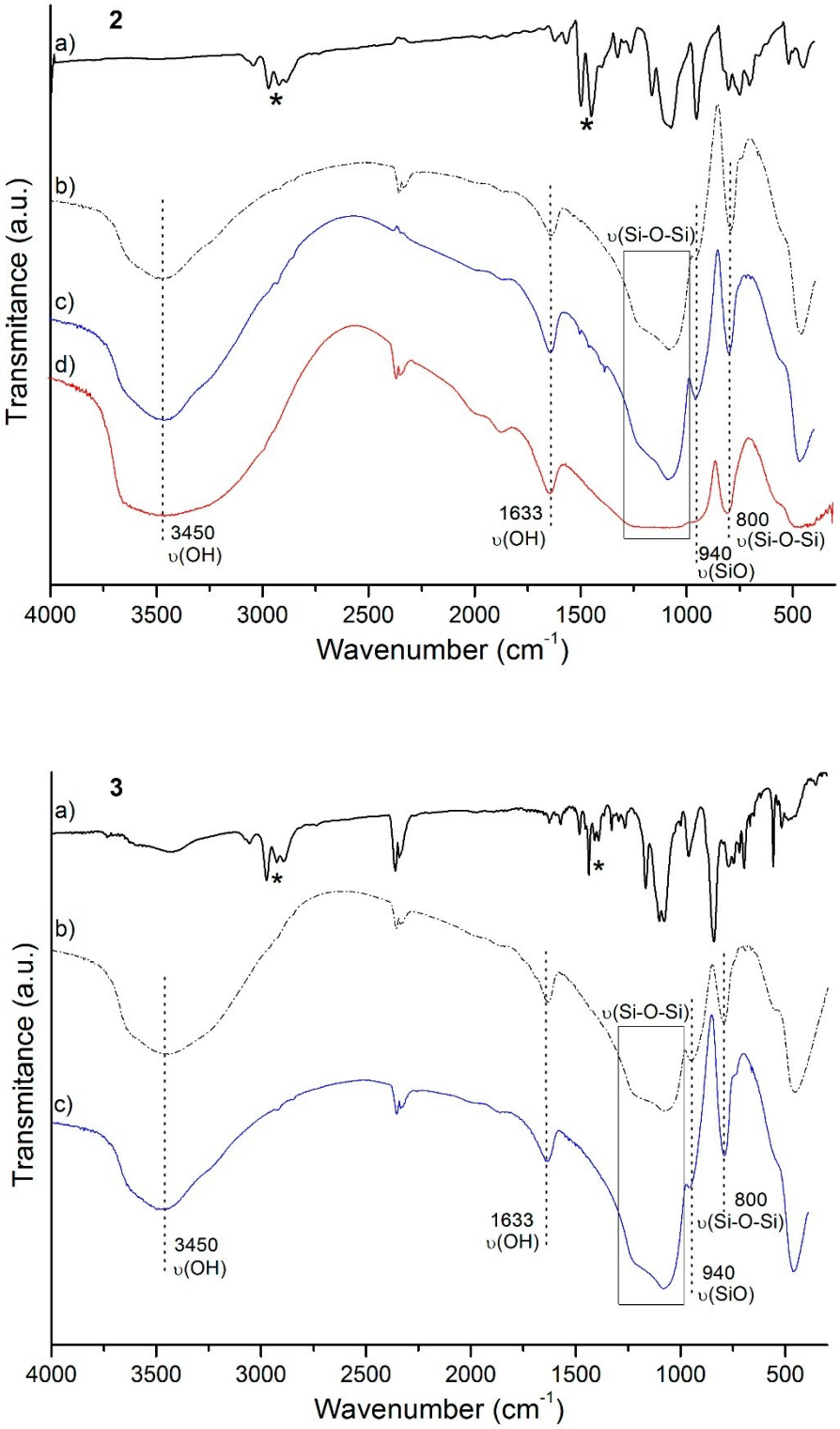

Figure S2. FTIR spectra of organometallo-silicas **[2,3]-SiO_2-P** (c) and **[2]-SiO_2-G** (d) in comparison with the spectra of the pure complexes **2** and **3** (a) and the control **complex-free silica SiO_2-P** (b). (*) Characteristic absorption of the complexes observed in the hybrid materials.

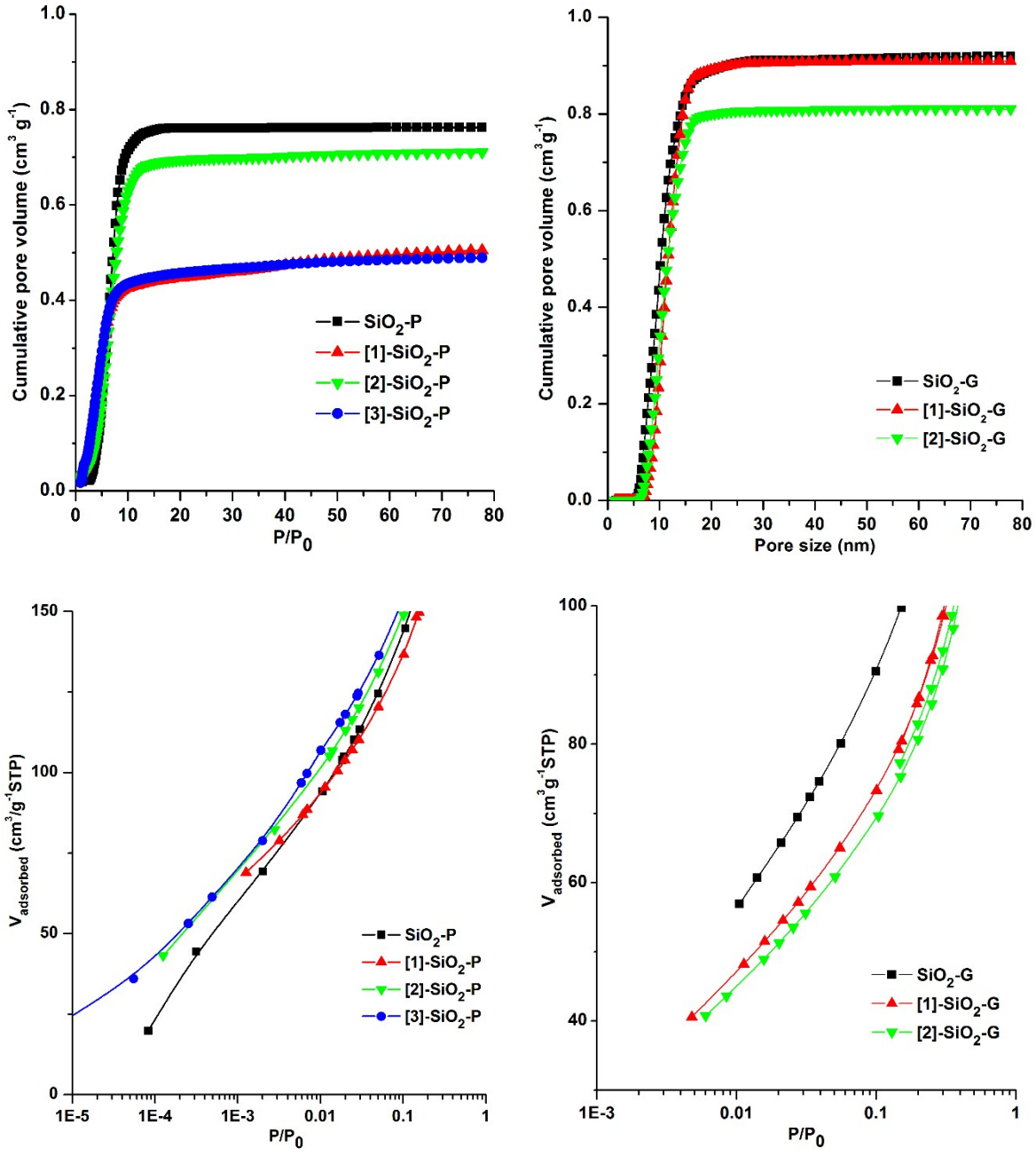

Figure S3. (Top) Cumulative pore volumes of organometallo-silica powders (left) and gels (air dried, right) in comparison with the related complex-free control silicas, calculated from the adsorption branch of the N_2 adsorption/desorption isotherms at 77K using the NLDFT method (see General Methods). (Bottom) Adsorption/desorption N_2 isotherms at 77K in a logarithmic P/P_0 scale.

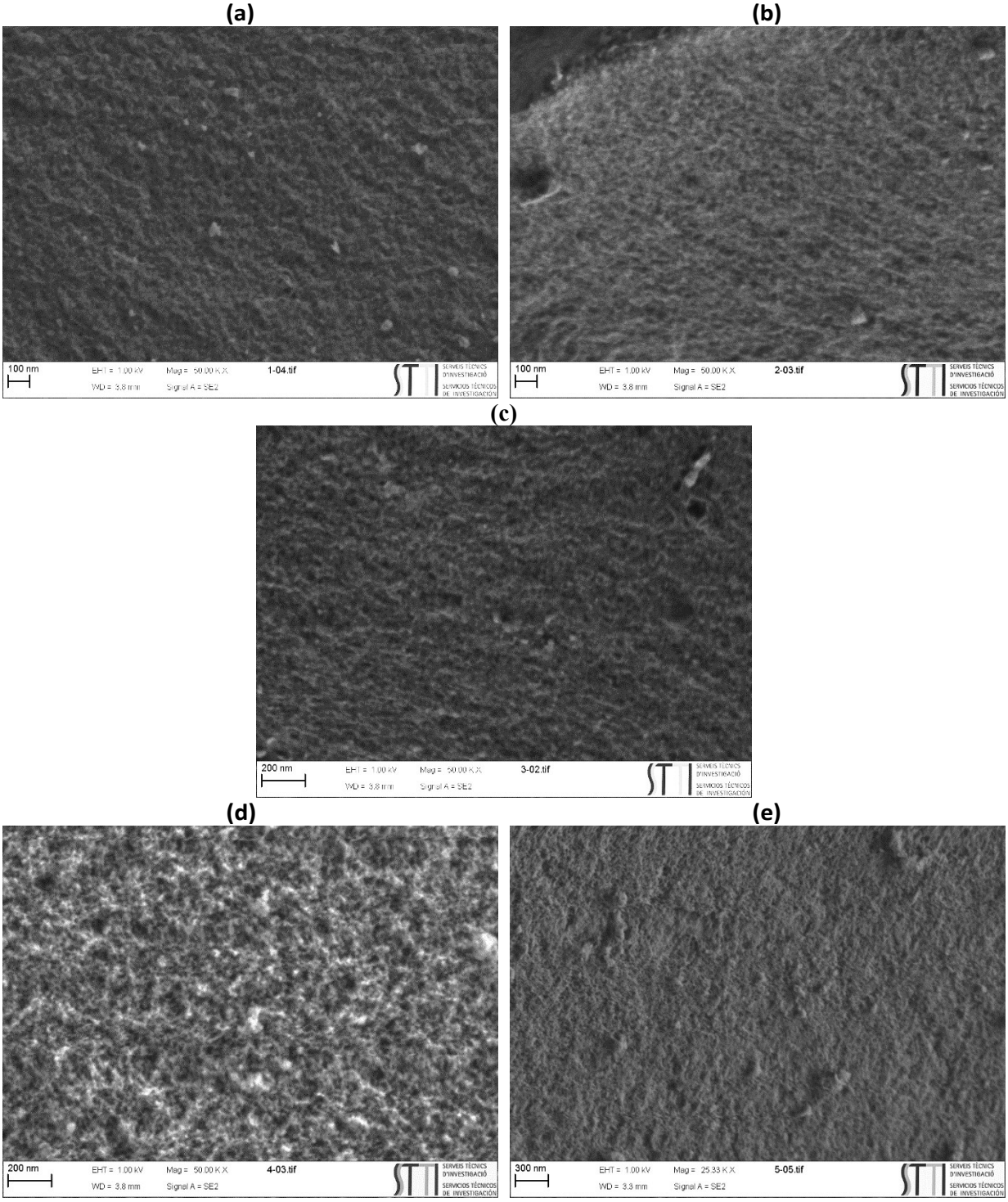

Figure S4. Representative FE-SEM images of **[1]-SiO_2-P** (a), **[2]-SiO_2-P** (b)**, [3]-SiO_2-P** (c)**, [1]-SiO_2-G** (d) and **[2]-SiO_2-G** (f).

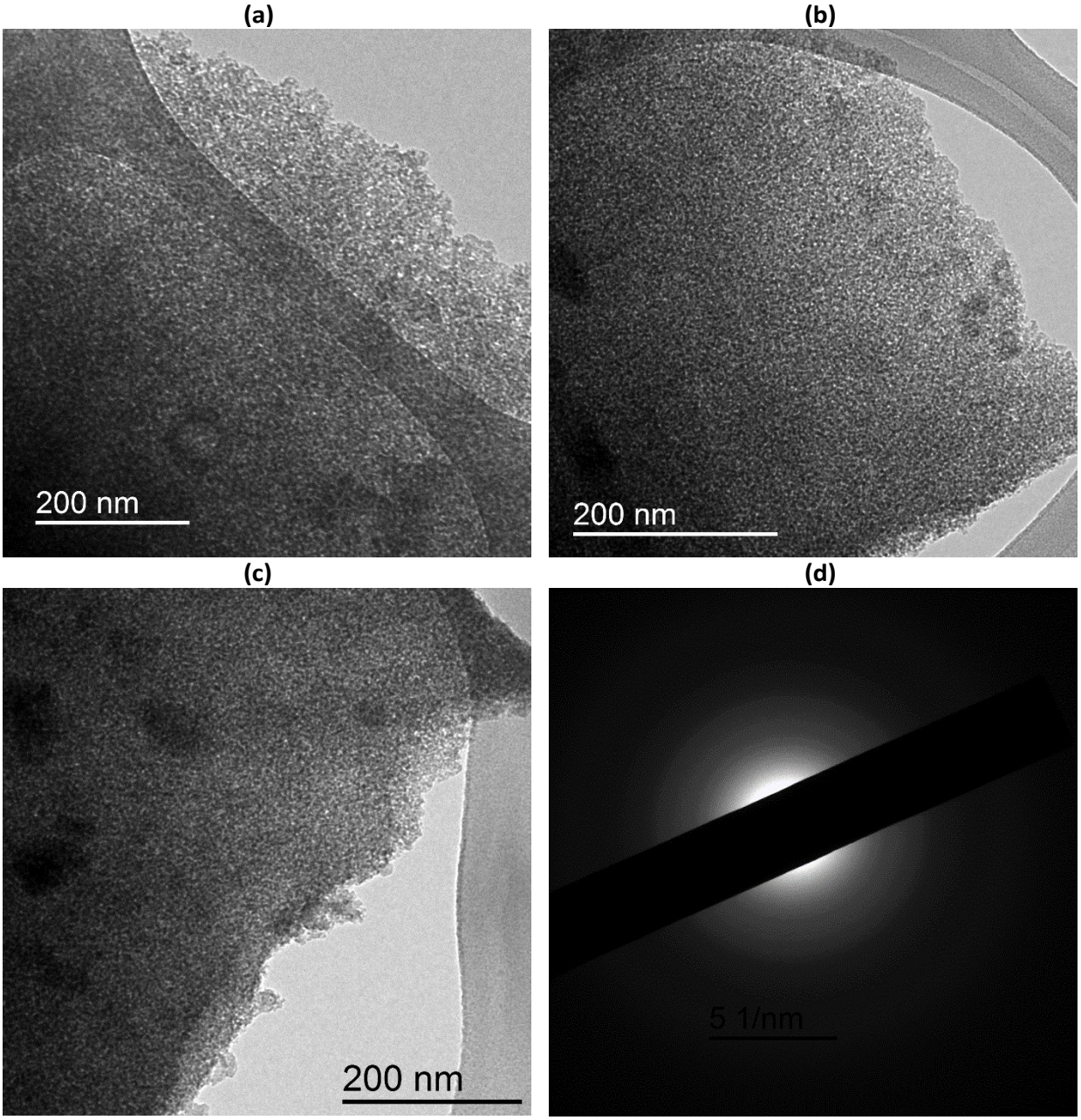

Figure S5. Representative TEM images of **[1]-SiO_2-P** (a), **[2]-SiO_2-P** (b) and **[3]-SiO_2-P** (c)**;** and the electron diffraction pattern of **[3]-SiO_2-P** (d)**.**

Table S2. Emission data of complexes **1**-**3** in solid state and solution (THF or CH_2Cl_2, 5 x 10^{-4} M) and of their hybrid silica materials (**[1-3]-SiO_2-P** and **[1,2]-SiO_2-G**).

Sample	Medium (T/K)	λ_{em}/ nm (λ_{ex}/ nm)	τ/μs	ϕ/ %
1	Solid (298)	512 (365)	0.97	31.2
	Solid (77)	463, 480, 504_{max}, 530_{sh} (365)	15.8 (460)	
	THF (298)	464, 494_{max}, 520_{sh} (365)	0.27 (460)	3.4
	THF (77)	460_{max}, 493, 519_{sh} (365)	44.0 (460)	
1% PMMA	Solid (298)	460, 495_{max}, 520_{sh} (365)	2.0 (460)	28.3
10% PMMA	Solid (298)	465, 500_{max}, 525_{sh} (365)		29.8
50% PMMA	Solid (298)	465, 500_{max}, 530_{sh} (365)		36.4
70% PMMA	Solid (298)	465, 510_{max}, 530_{sh} (365)		38.7
[1]-SiO_2-P	Solid (298)	510 (365)	0.93	6.9
	Solid (77)	480, 506_{max}, 538_{sh} (365)	21.4 (480)	
[1]-SiO_2-G[a)]	Solid (298)	465, 495_{max}, 515_{sh} (365)	0.79 (460)	8.5
	Solid (77)	460, 485_{max}, 515_{sh} (365)	40.4 (460)	
2[b)]	Solid (298)	485_{max}, 520, 560, 610_{sh} (365)	206,5	43.4
	Solid (77)	483_{max}, 520, 565, 610_{sh} (365)	378,3	
	CH_2Cl_2 (298)	497, 527_{max}, 570_{sh} (365)	0.66	2.0
	CH_2Cl_2 (77)	483, 517_{max}, 555 (365)	511	
PMMA (1%)	Solid (298)	485_{max}, 515, 560_{sh} (365)	146.7	7.6
	Solid (77)	480_{max}, 510, 555_{sh} (365)	798.0	
PMMA (10%)	Solid (298)	485_{max}, 515, 560_{sh} (365)		12.2
PMMA (50%)	Solid (298)	485_{max}, 515, 560_{sh} (365)		25.4
[2]-SiO_2-P	Solid (298)	485_{max}, 520, 560, 610 (365)	207,5	13.7
	Solid (77)	483_{max}, 520, 560, 610 (365)	404,8	
[2]-SiO_2-G[a)]	Solid (298)	487_{max}, 523, 561, 615 (365)	405.7	8.8
	Solid (77)	483, 520_{max}, 550, 600 (365)	1617.5	
3[c)]	Solid (77)	$493_{máx}$, 523, 552_{sh} (365)	536.9 (500)	
	THF (77)	477_{max}, 514, 550_{sh} (365)	1216 (480)	
PMMA 1%	Solid (298)	475_{max}, 500 (365)	84.3 (500)	2.0
	Solid (77)	480_{max}, 510, 550_{sh} (365)	650.2 (480)	
[3]-SiO_2-P	Solid (298)	$469_{máx}$, 495, 505 (365)	0.35 (470)	0.5
	Solid (77)	472, $501_{máx}$, 526_{sh} (365)	542.8 (500)	

a) Data for air dried **[1,2]-SiO_2-G** solids. Identical data were obtained for the transparent gels. b) No emissive in THF. c) No emissive at room temperature.

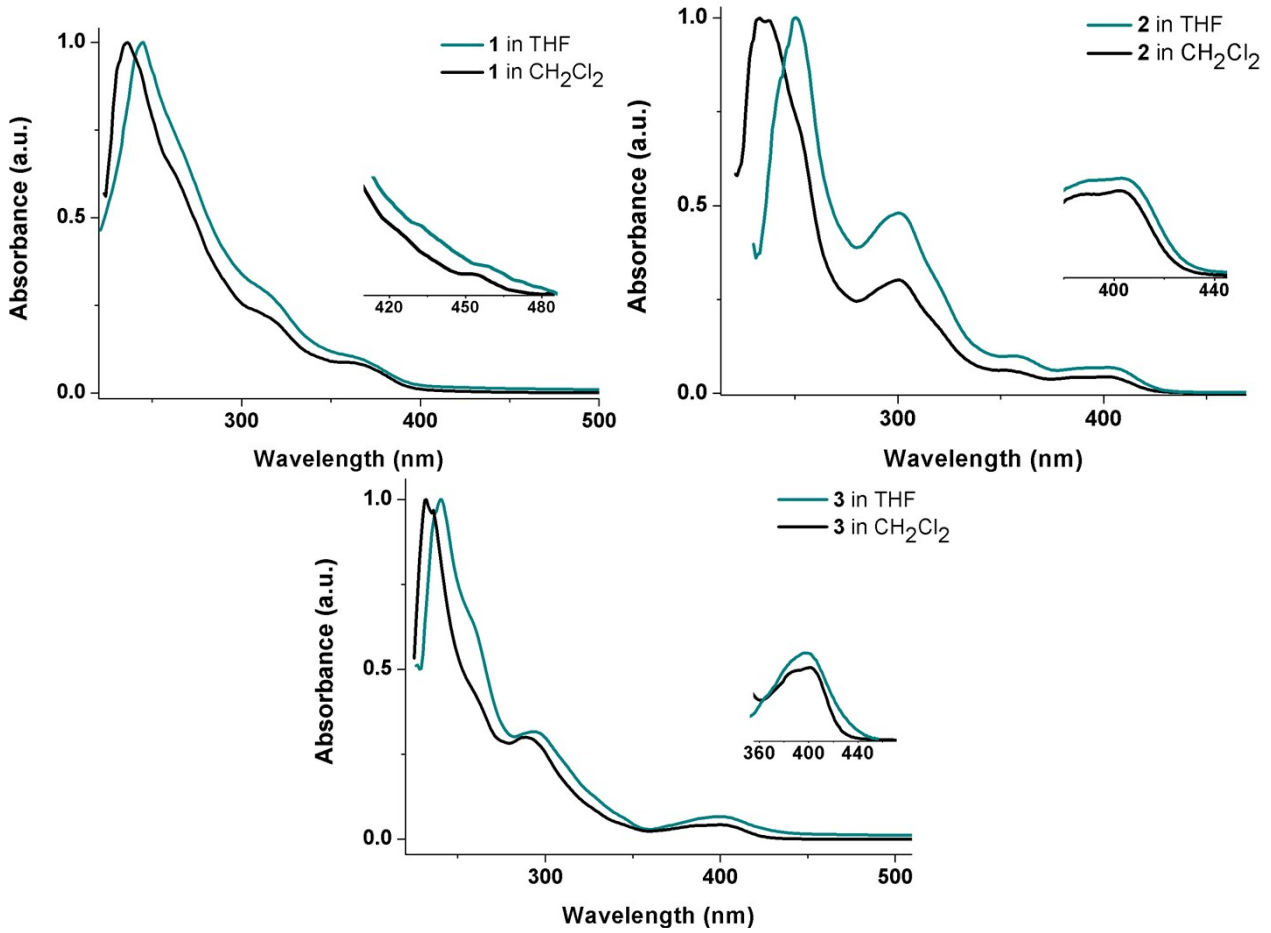

Figure S6. Absorption spectra of complexes **1** - **3** in THF and in CH_2Cl_2 (5 x 10^{-5} M).

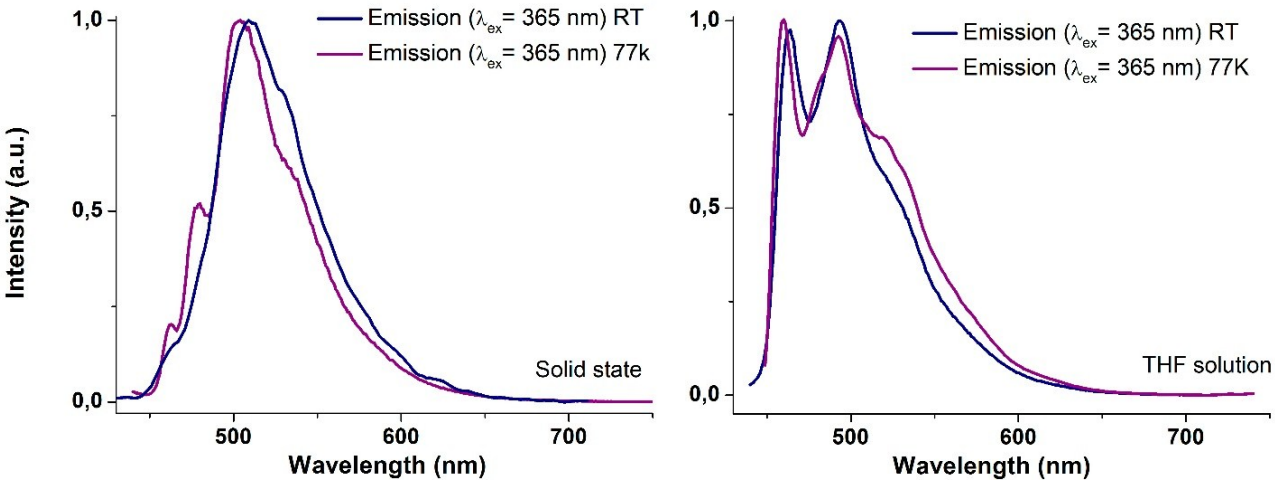

Figure S7. Emission spectra of complex **1** in solid state (left) and in THF solution (right, 5 x 10^{-4} M), at room temperature and at 77K.

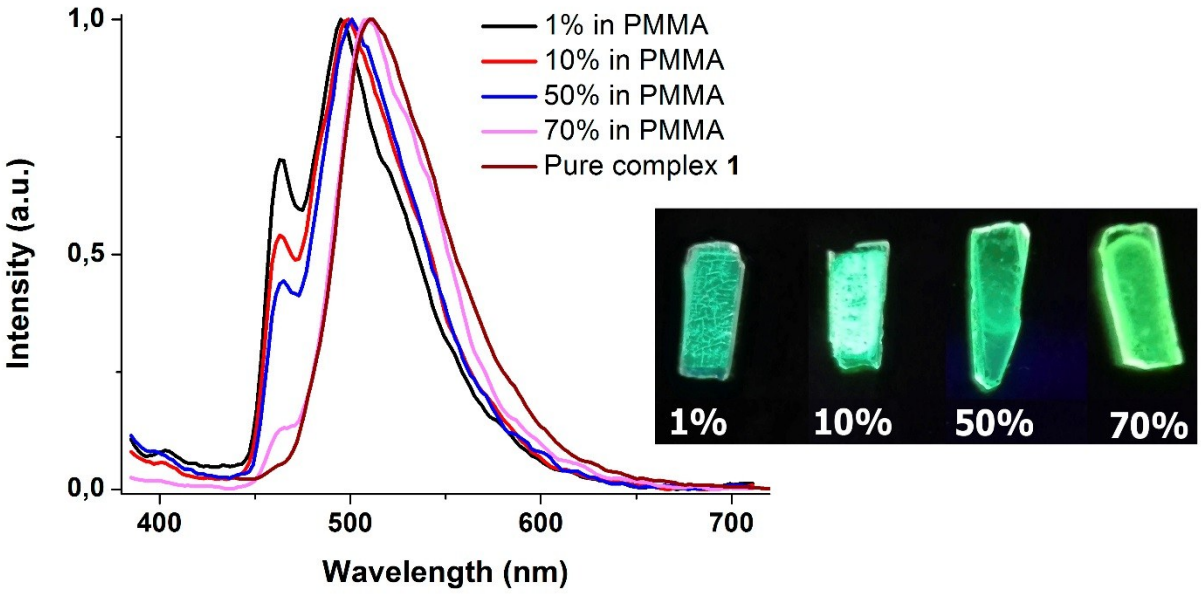

Figure S8. Normalized emission spectra of different concentrations of complex **1** in PMMA at room temperature.

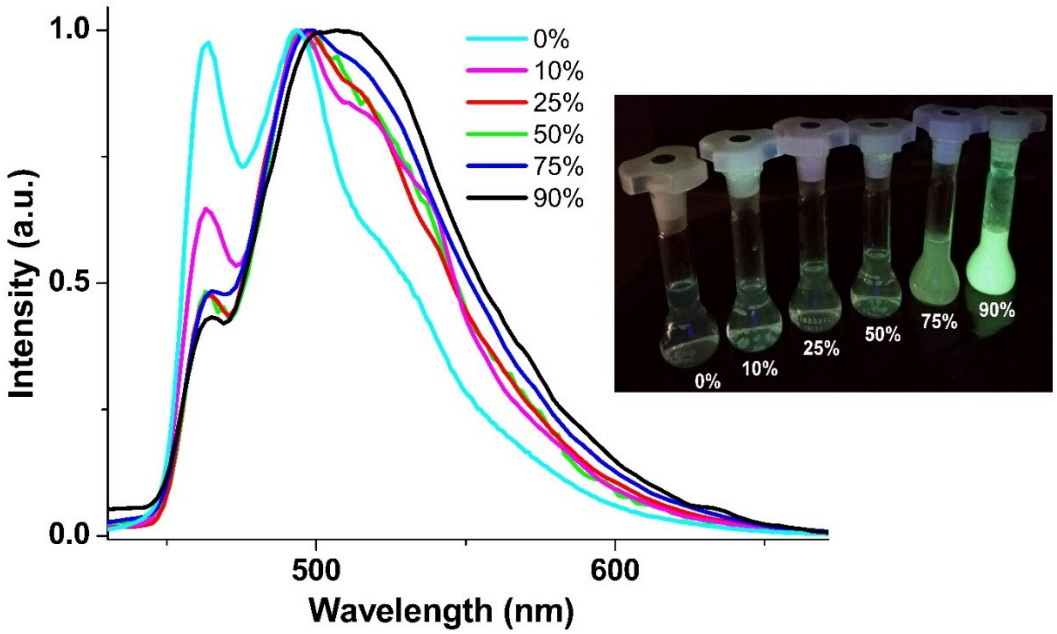

Figure S9. Normalized emission spectra of complex **1** in THF-H_2O mixtures with different water fractions (0-90 vol%).

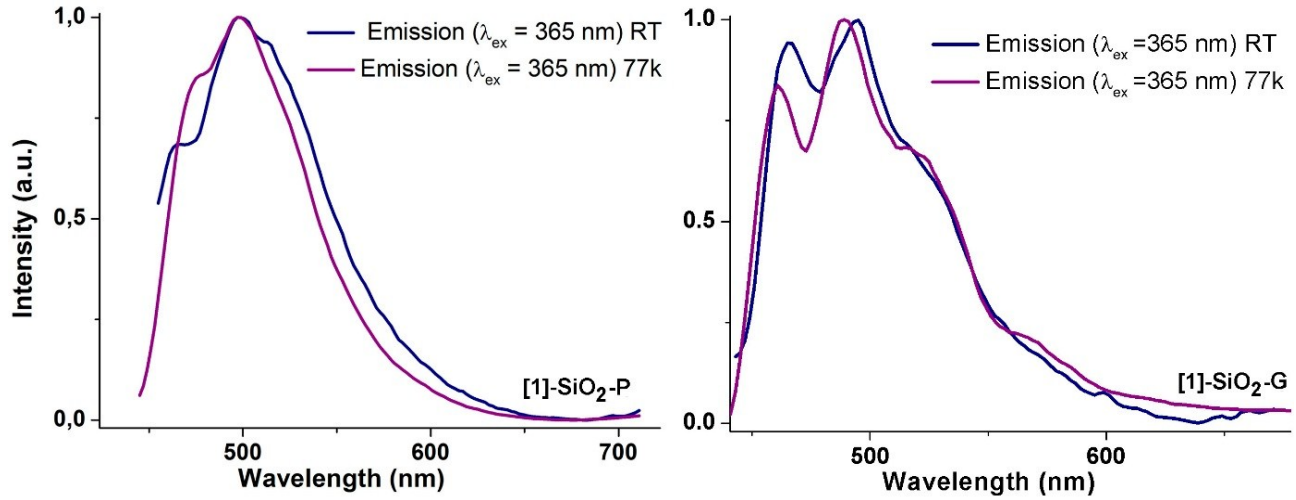

Figure S10. Emission spectra of **[1]-SiO_2-P** (left) and **[1]-SiO_2-G** (right) at room temperature and at 77K.

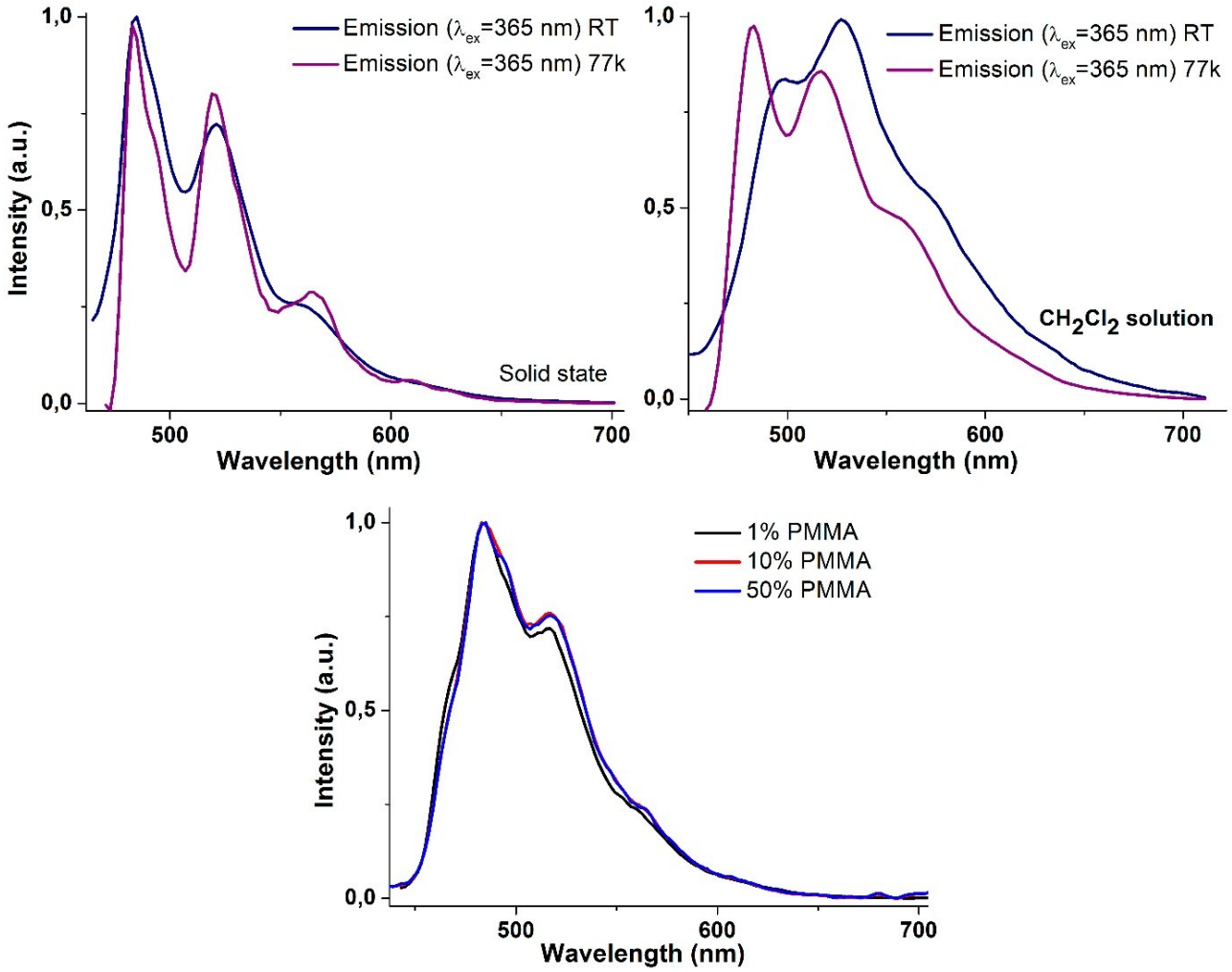

Figure S11. Emission spectra of complex **2** in solid state (left) and THF solution (right) at room temperature and 77K and in PMMA at room temperature (bottom).

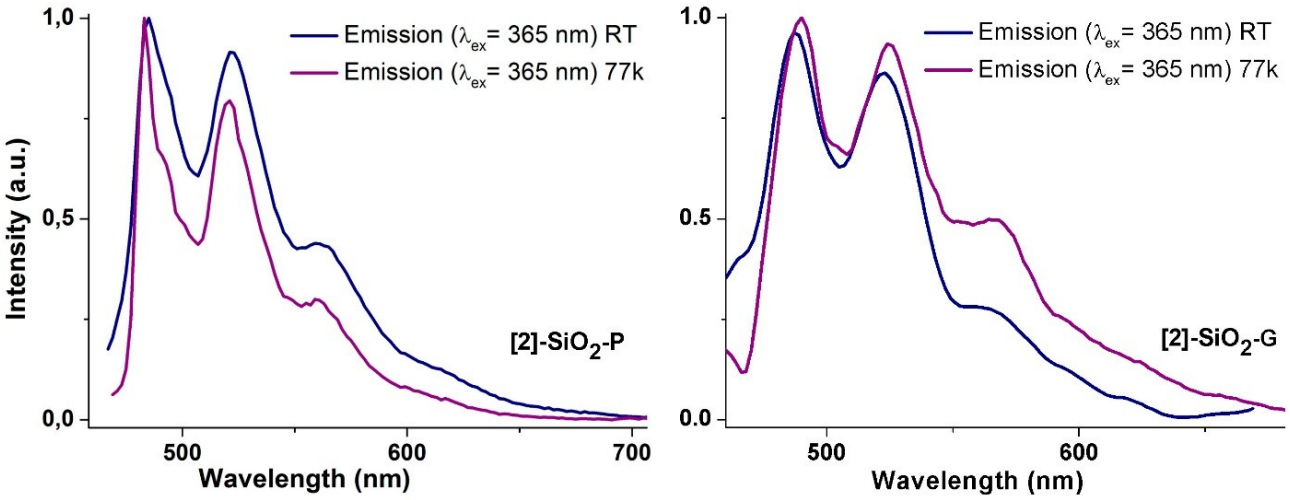

Figure S12. Emission spectra of **[2]-SiO_2-P** (left) and **[2]-SiO_2-G** (right) at room temperature and 77K.

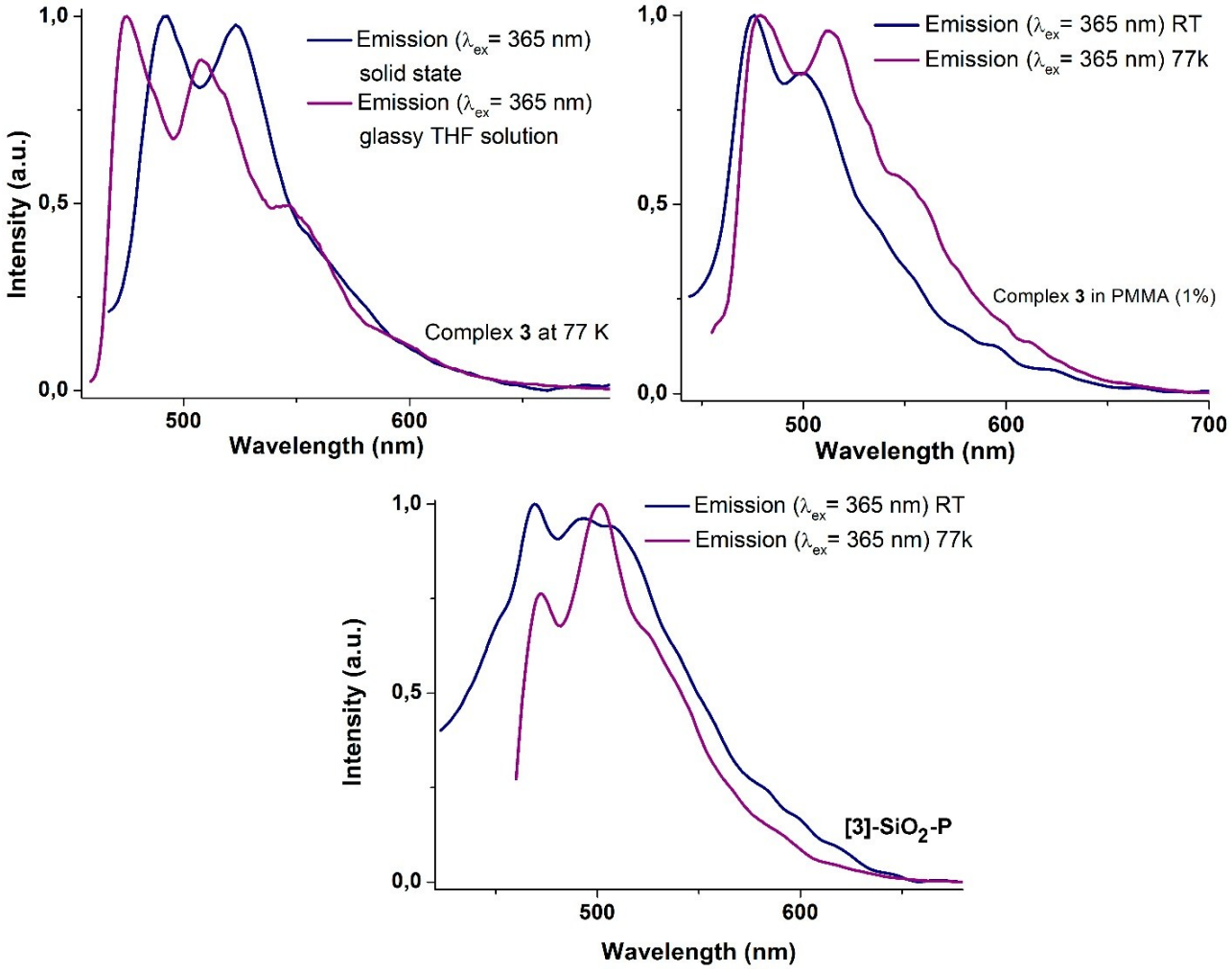

Figure S13. Emission spectra of complex **3** at 77K (left) in solid state (blue) and in glassy THF solution (5 x 10^{-4} M, purple), of complex **3** in PMMA (1%, right) and of **[3]-SiO_2-P** (bottom).

Theoretical calculations

Methods

Calculations for complex **1** were carried out with the Gaussian 09 package[5] using Becke's three-parameter functional combined with Lee-Yang-Parr's correlation functional (B3LYP) in the singlet state (S_0) and the unrestricted U-B3LYP in the triplet state (T_1).[6] According to previous theoretical calculations for iridium complexes, the optimized ground state geometry were calculated at the B3LYP/LANL2DZ (Ir)/6-31G(d,p) (ligand atoms) level. The S_0 geometry was found to be a true minimum as no negative frequencies in the vibrational frequency study of the final geometry were found. DFT and TD-DFT calculations were carried out using the polarized continuum model approach implemented in the Gaussian 09 software. The MO diagrams and the orbital contributions were generated with Gaussian 09 software and Gauss-Sum[7] program, respectively. The emission energy was calculated as the difference of the optimized T_1 geometry for both states.

Discussion

For complex **1**, the optimized geometry reproduces most of the details of the calculated and experimental values of a similar iridium compound ($[Ir(ppy)_2(PPh_3)(P(OPh)_3)]$)[8] with a reasonable agreement. Its analysis shows a good accuracy for the Ir-C, Ir-N and Ir-P bond lengths (maxima deviations of 0.2A) and no more than 5° of deviation was found between our complex bond angles and those reported.

Figure S15 displays the experimental and calculated (bars) absorption spectra in THF for complex **1**, which presents weak low energy singlet excitations (S1 375, S2 358 and S4 325 nm, Table S4) that are related to HOMO, H-1, LUMO and L+1 transitions. The target orbitals LUMO and LUMO+1 are distributed over both C^N ligands (ppy) (95% and 93%, respectively), whereas the HOMO is primarily located in the iridium center (36%) with some C^N contribution (61%), and HOMO-1 is only formed by C^N ligands (85%). Therefore, these absorptions are attributed to metal-ligand (^{1}MLCT, Ir→C^N) charge transfer transition with some intraligand ^{1}IL (C^N) contribution. More intense singlet excitations are predicted at higher energies (270 and 320 nm, LL'CT/MLCT). The lowest triplet state at the ground state geometry (T_1) results from a mixed of MLCT (Ir→C^N) and IL (C^N) transitions. Geometry optimization was also carried out by spin-unrestricted DFT calculations. The spin density at the optimized T_1 state is primary localized on one ppy ligand and on the metallic center, supporting so the ^{3}IL/^{3}MLCT assignment.

To obtain additional information about the emitting state, its behavior has also been proven by optimization of the lowest energy triplet state (T_1) using unrestricted U-B3LYP method (Table S6, Figures S17 and S18). The calculated electronic energies regarding to the ground state (512 nm) are red shifted in comparison to the experimental value (464 nm, THF) owing to insufficient description of the charge-transfer transitions using DFT calculations. The SOMO orbital is mainly analogous to the LUMO in the ground state in spite now it is only distributed on one C^N ligand (93%); whereas the SOMO-1 is essentially similar to the HOMO in the S_0 state,

located on the iridium center (14%) and just in one C^N ligand (84%). Therefore, the emission is attributed to a ^{3}IL (C^N) transition mixed with ^{3}MLCT (Ir→C^N) character.

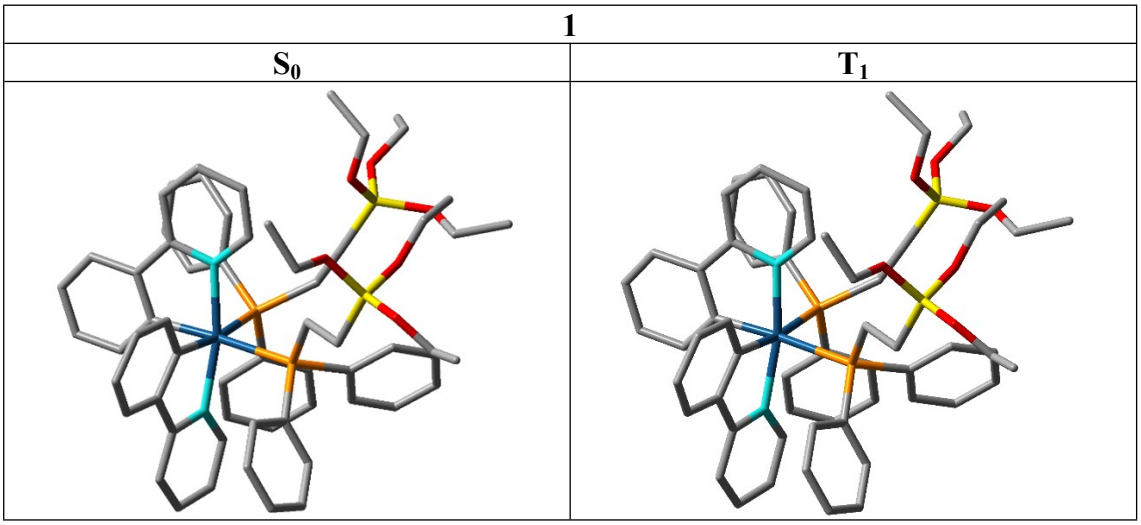

Figure S14. Optimized structures of S_0 and T_1 states of complex **1**.

Table S3. DFT optimized geometries for ground state and triplet state of complex **1.**

	S_0	T_1	S_0[a]	X-Ray[a]
Ir(1)-N(1)	2.108	2.112	2.114	2.042
Ir(1)-N(1')	2.109	2.072	2.111	2.089
Ir(1)-C(10)	2.053	2.046	2.062	2.072
Ir(1)-C(10')	2.050	2.031	2.060	2.071
Ir(1)-P(1)	2.587	2.596	2.419	2.307
Ir(1)-P(1')	2.588	2.614	2.593	2.433
N(1)-Ir(1)-N(1')	167.32	168.28	167.05	164.34
N(1)-Ir(1)-C(10)	79.03	79.09	79.42	78.97
N(1')-Ir(1)-C(10')	79.18	80.49	79.44	79.06
N(1)-Ir(1)-C(10')	91.86	91.69		
N(1')-Ir(1)-C(10)	91.07	91.49		
P(1)-Ir(1)-P(1')	100.38	100.08	95.73	95.19
P(1)-Ir(1)-N(1)	85.99	85.61		
P(1)-Ir(1)-C(10)	87.61	87.58		
P(1)-Ir(1)-N(1')	101.63	101.09		
P(1)-Ir(1)-C(10')	171.91	172.74	175.39	177.04
P(1')-Ir(1)-N(1)	104.03	104.10		
P(1')-Ir(1)-C(10)	171.57	171.85	171.32	169.33
P(1')-Ir(1)-N(1')	84.74	84.35		
P(1')-Ir(1)-C(10')	87.70	87.12		

[a.] Corresponding data to complex $[Ir(ppy)_2(PPh_3)(P(OPh)_3)]$[8b]

Table S4. Selected vertical excitation energies singlets (S_0) and first triplets computed by TDDFT/SCRF (THF) with the orbitals involved for complex **1**.

State	λ_{ex}(calc)(nm)	f	Major transition (% Contribution)	Main Character
T_1	439.14	0.0	H-1->L+1 (15%), HOMO->LUMO (48%)	MLCT/IL
T_2	434.54	0.0	H-1->LUMO (30%), HOMO->L+1 (30%)	MLCT/IL
S_1	375.51	0.0427	HOMO->LUMO (97%)	MLCT/IL
S_2	357.69	0.0014	HOMO->L+1 (97%)	MLCT/IL
S_4	325.28	0.0311	H-1->L+1 (89%)	IL
S_5	317.34	0.0253	HOMO->L+2 (90%)	MLCT/IL
S_6	310.22	0.0361	H-5->LUMO (18%), H-3->LUMO (49%), H-2->LUMO (20%)	IL
S_8	307.64	0.0178	H-4->LUMO (29%), HOMO->L+3 (52%)	LL'CT/MLCT
S_9	304.19	0.0817	H-7->LUMO (10%), H-4->LUMO (37%), H-2->LUMO (35%)	LL'CT/IL
S_{10}	300.36	0.0245	H-7->LUMO (32%), H-5->LUMO (15%), H-2->L+1 (12%)	LL'CT/IL
S_{26}	270.83	0.0563	H-1->L+4 (62%)	LL'CT

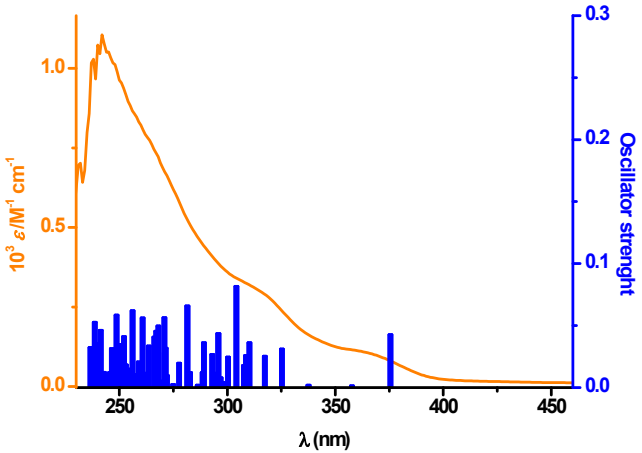

Figure S15. Calculated stick absorption spectra of Ir^{III} complex **1** in THF compared to the experimental one.

Table S5 Composition (%) of frontier MOs in the ground state for complex **1** in THF.

	eV	ppy(1)	ppy(2)	PPETS(1)	PPETS(2)	Ir
LUMO+5	-1.13	7	2	31	55	6
LUMO+4	-1.25	6	4	57	28	5
LUMO+3	-1.4	43	45	2	9	1
LUMO+2	-1.53	42	49	2	5	1
LUMO+1	-1.89	56	37	1	1	4
LUMO	-2.07	38	57	2	2	2
HOMO	-6.1	28	33	1	1	36
HOMO-1	-6.38	45	40	4	4	6
HOMO-2	-6.71	53	2	8	30	8
HOMO-3	-6.72	20	44	7	19	10
HOMO-4	-6.75	3	42	38	6	11
HOMO-5	-6.96	13	23	14	5	44

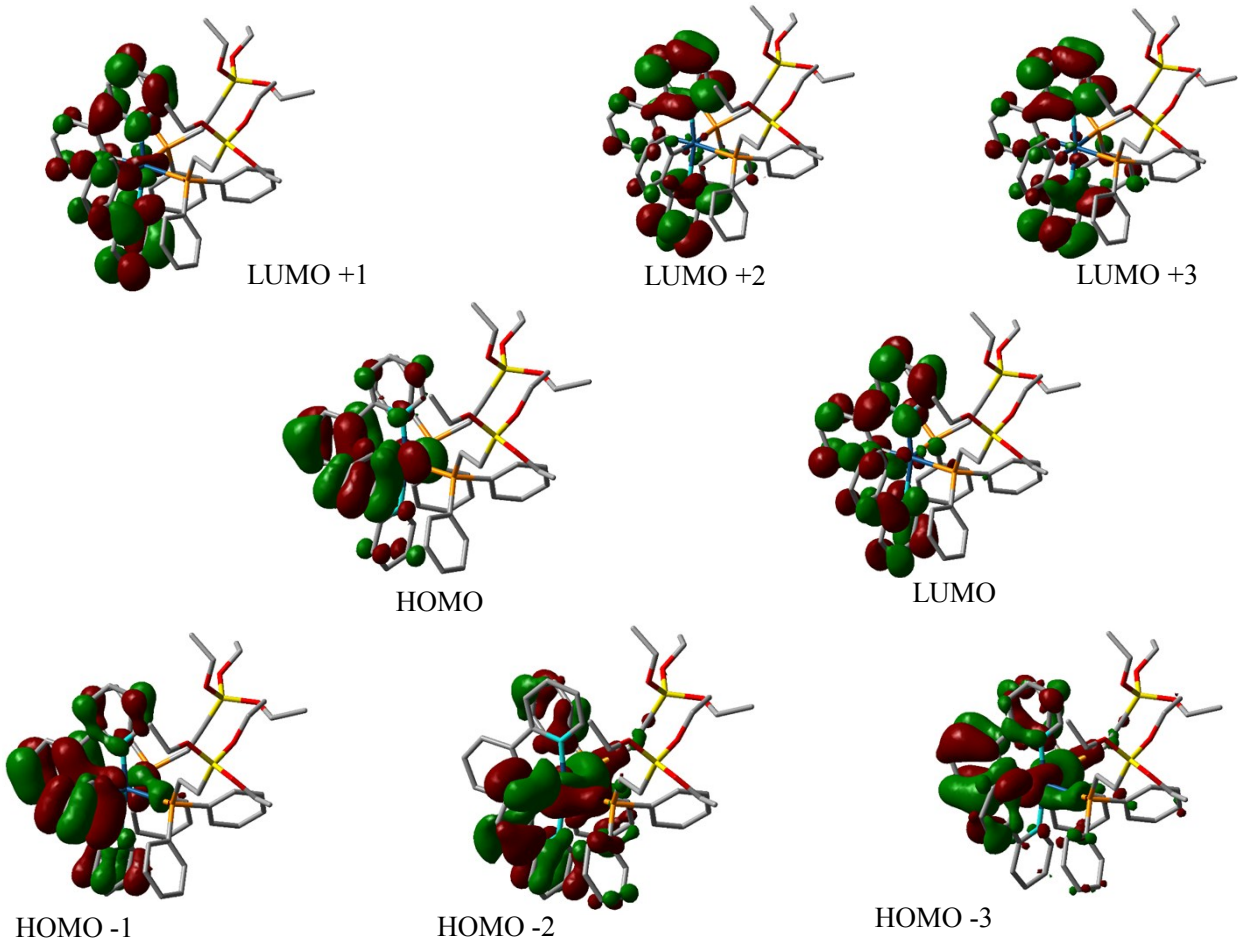

Figure S16. Selected frontier Molecular Orbitals for complex **1.**

Table S6. Composition (%) of frontier MOs in the first triple-state for compound **1** in THF.

	eV	ppy(1)	ppy(2)	PPETS(1)	PPETS(2)	Ir
SOMO	-3.61	1	93	0	2	3
SOMO-1	-4.64	1	84	0	1	14

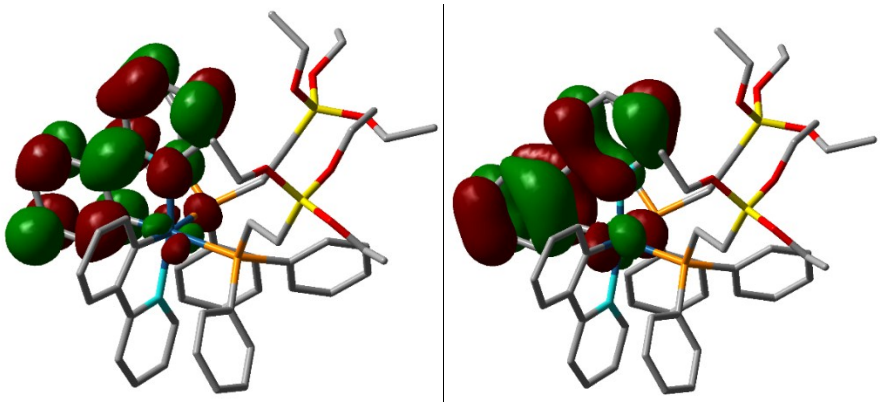

SOMO SOMO -1

Figure S17. SOMO and SOMO-1 orbitals for complex **1**.

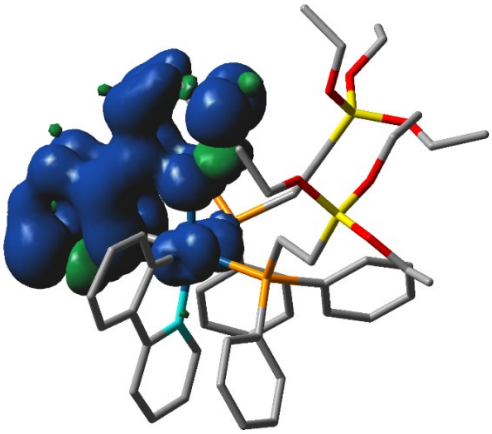

Spin density: 0.161829

Figure S18. Spin-density distributions calculated for the emitting excited state (T_1) of complex **1**.

Supplementary References

1. *British Standar. Pore size distribution ans porosity of solid materials by mercury porosimetry and gas adsorption.* , BS ISO 15901-3; 2007.
2. Z. Otwinowski and W. Minor, in *Methods in Enzymology*, eds. C. V. Carter, Jr. and R. M. Sweet, Academic Press, New York, 1997, vol. 276A, p. 307.
3. G. Sheldrick, *Acta Crystallogr. Sect. A*, 2015, **71**, 3-8.
4. G. Sheldrick, *Acta Crystallogr. Sect. C*, 2015, **71**, 3-8.
5. M. J. Frisch, G. W. Trucks, H. B. Schlegel, G. E. Scuseria, M. A. Robb, J. R. Cheeseman, G. Scalmani, V. Barone, B. Mennucci, G. A. Petersson, H. Nakatsuji, M. Caricato, X. Li, H. P. Hratchian, A. F. Izmaylov, J. Bloino, G. Zheng, J. L. Sonnenberg, M. Hada, M. Ehara, K. Toyota, R. Fukuda, J. Hasegawa, M. Ishida, T. Nakajima, Y. Honda, O. Kitao, H. Nakai, T. Vreven, J. A. Montgomery, J. E. Peralta, F. Ogliaro, M. Bearpark, J. J. Heyd, E. Brothers, K. N. Kudin, V. N. Staroverov, R. Kobayashi, J. Normand, K. Raghavachari, A. Rendell, J. C. Burant, S. S. Iyengar, J. Tomasi, M. Cossi, N. Rega, J. M. Millam, M. Klene, J. E. Knox, J. B. Cross, V. Bakken, C. Adamo, J. Jaramillo, R. Gomperts, R. E. Stratmann, O. Yazyev, A. J. Austin, R. Cammi, C. Pomelli, J. W. Ochterski, R. L. Martin, K. Morokuma, V. G. Zakrzewski, G. A. Voth, P. Salvador, J. J. Dannenberg, S. Dapprich, A. D. Daniels, Farkas, J. B. Foresman, J. V. Ortiz, J. Cioslowski and D. J. Fox, *Gaussian 09, Revision B.01*, Gaussian, Inc., Wallingford CT, , 2009.
6. a) C. Lee, W. Yang and R. G. Parr, *Phys. Rev. B*, 1988, **37**, 785-789; b) A. D. Becke, *J. Chem. Phys.*, 1993, **98**, 5648-5652; c) A. D. Becke, *Phys. Rev. A*, 1988, **38**, 3098-3100.
7. N. M. O'Boyle, A. L. Tenderholt and K. M. Langner, *J. Comput. Chem.*, 2008, **29**, 839-845.
8. a) X. Qu, Y. Liu, G. Godefroid, Y. Si, X. Shang, X. Wu and Z. Wu, *Eur. J. Inorg. Chem.*, 2013, **2013**, 3370-3383; b) C. S. Chin, M.-S. Eum, S. y. Kim, C. Kim and S. K. Kang, *Eur. J. Inorg. Chem.*, 2006, **2006**, 4979-4982.